

# Clustering Constraints on the Relative Sizes of Central and Satellite Galaxies

Andrew Hearin<sup>1</sup>, Peter Behroozi<sup>2</sup>, Andrey Kravtsov<sup>3</sup>, Benjamin Moster<sup>4</sup>

<sup>1</sup>*Argonne National Laboratory, Argonne, IL, USA 60439, USA*

<sup>2</sup>*Department of Physics, University of Arizona, 1118 E 4th St, Tucson, AZ 85721 USA*

<sup>3</sup>*Department of Astronomy & Astrophysics, The University of Chicago, Chicago, IL 60637 USA*

<sup>4</sup>*Universitäts-Sternwarte, Ludwig-Maximilians-Universität München, Scheinerstr. 1, 81679 München, Germany*

6 November 2017

## ABSTRACT

We place empirical constraints on the connection between dark matter halos and galaxy half-light radii,  $R_{1/2}$ . Low-redshift SDSS measurements show that smaller galaxies cluster much more strongly than larger galaxies at fixed stellar mass. Using `Halotools` to forward model the observations, we find that the clustering signal generically requires satellite galaxies to be smaller than central galaxies of the same halo mass. We present a simple empirical model consistent with the clustering results, in which galaxy size is proportional to halo virial radius at the time of peak halo mass. We use this model to predict how galaxy lensing,  $\Delta\Sigma$ , should depend on  $R_{1/2}$  for  $M_*$ -complete samples. Other simple empirical models fail the clustering test, such as models in which galaxy size is related to stellar mass alone; these failures persist even when accounting for possible effects from satellite stripping and orphan galaxies. Our results suggest that the relative size of centrals and satellites is predetermined at the time of satellite infall, and that a remarkably simple galaxy–halo scaling relation emerges from the complex physics regulating galaxy size.

## 1 INTRODUCTION

Many properties of observed galaxies exhibit remarkably tight scaling relations. Galaxy size, typically quantified by a half-mass or half-light radius,  $R_{1/2}$ , has well-measured scaling with galaxy mass  $M_*$  in the local Universe (Shen et al. 2003; Guo et al. 2009; Huang et al. 2013; Lange et al. 2015; Zhang & Yang 2017), and at higher redshift (Trujillo et al. 2004; van der Wel et al. 2014; Kawamata et al. 2015; Shibuya et al. 2015; Huertas-Company et al. 2013; Huang et al. 2017). Observational constraints on models for galaxy  $R_{1/2}$  typically come from one-point function measurements such as  $\langle R_{1/2}|M_* \rangle_{\text{median}}$  and  $\sigma(R_{1/2}|M_*)$ , e.g., Khochfar & Silk (2006); Desmond et al. (2017); Bottrell et al. (2017); Hou et al. (2017); Somerville et al. (2017), or otherwise from catalogs of galaxy groups (Weinmann et al. 2009; Huertas-Company et al. 2013; Spindler & Wake 2017). Observations of two-point galaxy clustering,  $w_p(r_p)$ , have historically been used to place tight constraints on many features of the galaxy–halo connection, such as its  $M_*$ -dependence (Moster et al. 2010; Leauthaud et al. 2012; Reddick et al. 2013; Skibba et al. 2015), dependence on luminosity (Tinker et al. 2005; Cacciato et al. 2013), broadband color (Coil et al. 2008; Zehavi et al. 2011; Guo et al. 2011; Hearin & Watson 2013), and star-formation rate (Wang et al. 2007; Tinker et al. 2013; Watson et al. 2015). In the present work, we exploit the constraining power of  $w_p(r_p)$

to test empirical models connecting galaxy  $M_*$  and  $R_{1/2}$  to the properties of the galaxy’s parent dark matter halo.

## 2 DATA AND SIMULATIONS

Using galaxies observed in the Sloan Digital Sky Survey (SDSS) with the stellar mass measurements taken from the MPA-JHU catalog (Kauffmann et al. 2003; Brinchmann et al. 2004), we define volume-limited samples of galaxies according to the same  $M_*$ -completeness cuts used in Behroozi et al. (2015) (see Figure 2). We supplement the MPA-JHU catalog with measurements of half-light radius,  $R_{1/2}$ , derived from galaxy profile decompositions provided by Meert et al. (2015). The Meert et al. (2015) catalog is based on Data Release 10 of SDSS (Ahn et al. 2014), with improvements to the photometry pipeline and light profile fitting methods (Vikram et al. 2010; Bernardi et al. 2013, 2014; Meert et al. 2013). In the version of this catalog that we use,<sup>1</sup> two-dimensional

<sup>1</sup> Our  $M_*$  and  $R_{1/2}$  measurements are derived from different photometry pipelines; this is driven by our desire for consistency with the Behroozi et al. (2015) completeness cuts used in our clustering measurements. We note that we have repeated our analysis for stellar mass measurements based on  $?$ , finding only minor quantitative, and no qualitative changes to our results.

$r$ -band profiles were fit with a two-component de Vaucouleurs + exponential profile to determine the half-light radius of total  $r$ -band luminosity,  $R_{1/2}$ .

As the bedrock of our modeling, we use the publicly available<sup>2</sup> catalog of *Rockstar* subhalos identified at  $z = 0$  in the Bolshoi-Planck simulation (Klypin et al. 2011; Behroozi et al. 2013, ?; Riebe et al. 2013; Rodríguez-Puebla et al. 2016). As described in §3.1, we will use traditional abundance matching to connect stellar mass  $M_*$  with subhalo peak mass  $M_{\text{peak}}$ . To address issues related to subhalo incompleteness (Guo & White 2014; Campbell et al. 2017), we supplement the Bolshoi-Planck subhalo catalog with *all* subhalos that were ever identified by *Rockstar*, including those that no longer appear in the standard catalog as subhalos that survive to  $z = 0$ . We describe our treatment of these “orphan” subhalos in the Appendix.

For our SDSS galaxy samples, we calculate two-point clustering  $w_p$  using line-of-sight projection of  $\pi_{\text{max}} = 20$  Mpc using the *correl* program in *UniverseMachine*. For mock galaxies, to compute galaxy clustering we employ the distant observer approximation by treating the simulation  $z$ -axis as the line-of-sight. We compute  $w_p$  using the *mock\_observables.wp* function in *Halotools* (Hearin et al. 2016), which is a python implementation of the algorithm in the *Corrfunc* C library (Sinha & Garrison 2017). We also use *Halotools* to compute the galaxy-galaxy lensing signal,  $\Delta\Sigma$ , using the *mock\_observables.delta\_sigma* function.

All numerical values of  $R_{1/2}$  will be quoted in physical kpc, and all values of  $M_*$  and  $M_{\text{halo}}$  in  $M_\odot$ , assuming  $H_0 = 67.8 \text{ km/s} \equiv 100h \text{ km/s}$ , the best-fit value from Planck Collaboration et al. (2016). To scale stellar masses to “ $h = 1$  units” (Croton 2013), our numerically quoted values for  $M_*$  should be multiplied by a factor of  $h^2$ , while our halo masses and distances should be multiplied by a factor of  $h$ .

## 2.1 Classifying large vs. small galaxies

Because galaxy clustering has well-known dependence upon  $M_*$  that is not the subject of this work, we wish to remove this influence and focus purely on the relationship between  $R_{1/2}$  and  $w_p(r_p)$ . To do so, we determine the value  $\langle R_{1/2} | M_* \rangle_{\text{median}}$  by computing a sliding median of  $R_{1/2}$  for galaxies sorted by  $M_*$ , calculated using a window of width  $N_{\text{gal}} = 1000$ . Each galaxy is categorized as either “large” or “small” according to whether it is above or below the median value appropriate for its stellar mass. We note that this is analogous to the common convention for studying the properties of “red” vs. “blue” galaxies, in which the two subsamples are divided by a  $M_*$ - or luminosity-dependent green valley cut (e.g., van den Bosch et al. 2008; Zehavi et al. 2011), only here the  $R_{1/2}$  distribution is uni-modal, not bi-modal.

Using this technique, for any  $M_*$ -threshold sample, the stellar mass function of the “large” and “small” subsamples are identical. We illustrate this for the particular

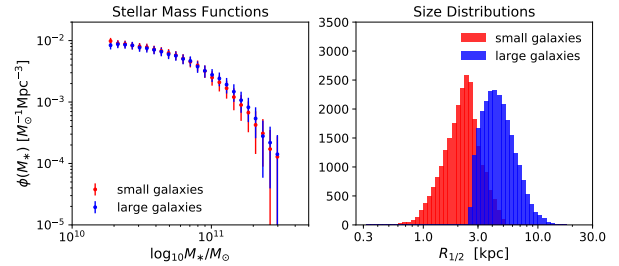


**Figure 1. Definition of “small” and “large” galaxies.** For a volume-limited SDSS galaxy sample defined by  $M_* > 10^{10.25} M_\odot$ , we visually demonstrate how we classify galaxies into “small” and “large” subsamples. As described in detail in §2.1, we compute the median value  $\langle R_{1/2} | M_* \rangle_{\text{median}}$  using a sliding window with a width of 1000 galaxies at each value of  $M_*$ . The *left panel* compares the stellar mass functions  $\phi(M_*)$  of the two samples, confirming that our method for separating “small” from “large” galaxies yields subsamples with statistically indistinguishable  $\phi(M_*)$ . The *right panel* shows histograms of  $R_{1/2}$  for the two subsamples, which partially overlap due to the finite range of  $M_*$  in the volume-limited sample.

case of  $M_* > 10^{10.25} M_\odot$  in left panel of Figure 1, which shows histograms of stellar mass for the two subsamples. The right panel of Figure 1 compares histograms of their size distributions, which partially overlap due to the variation in  $\langle R_{1/2} | M_* \rangle_{\text{median}}$  across the  $M_*$ - range of the threshold sample.

## 3 GALAXY-HALO MODEL

### 3.1 Abundance Matching

We map  $M_*$  onto subhalos using deconvolution abundance matching (SHAM). See section 3.3 of Behroozi et al. (2010) or the appendix of Kravtsov et al. (2014) for an account of the mathematics underlying this technique in the presence of scatter. To perform the abundance matching, we use the publicly available code<sup>3</sup> developed by Yao-Yuan Mao (Lehmann et al. 2017) that provides a python wrapper around the C kernel developed by Peter Behroozi (Behroozi et al. 2010). For the subhalo property used in SHAM, we use  $M_{\text{peak}}$ , the largest value of  $M_{\text{vir}}$  ever attained by the subhalo throughout the entire history of the main progenitor halo. Using the stellar mass function provided in Moustakas et al. (2013), we model  $M_*$  as a log-normal distribution with 0.2dex of scatter about the median relation  $\langle M_* | M_{\text{peak}} \rangle_{\text{median}}$  determined by SHAM. As described in the appendix, we include a prescription for supplementing the ordinary *Rockstar* subhalo catalog with disrupted subhalos, so that some of our model galaxies inhabit subhalos that are no longer resolved and do not appear in the standard publicly available catalog.

<sup>2</sup> [http://www.slac.stanford.edu/~behroozi/BPlanck\\_Hlists](http://www.slac.stanford.edu/~behroozi/BPlanck_Hlists)

<sup>3</sup> <https://bitbucket.org/yymao/abundancematching/overview>

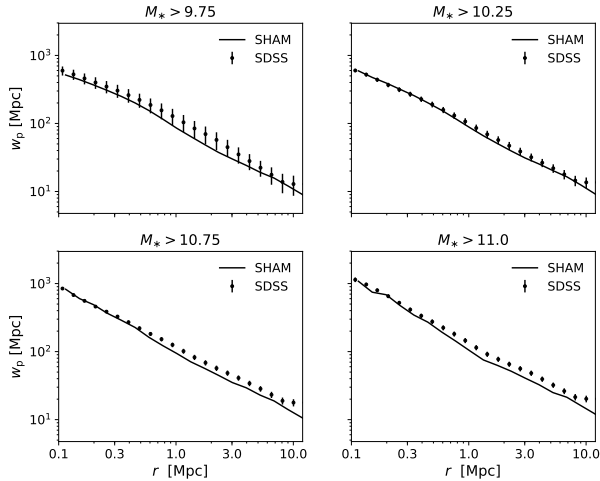


**Figure 2. Abundance matching clustering predictions.** Using the abundance matching methods described in §3.1, we compare the projected clustering of mock vs. SDSS galaxies. Each panel shows the comparison for a volume-limited sample defined by a different  $M_*$ -threshold. Black points with error bars show SDSS measurements; solid black curves show the abundance matching prediction of our fiducial model, which includes the effect of orphan subhalos (see Appendix A). Including orphans mitigates the discrepancy in the clustering predicted by traditional,  $M_{\text{peak}}$ -based SHAM based, though mild tension remains for  $M_* \gtrsim 10^{10.75} M_\odot$ .

### 3.2 Galaxy size models

In §4, we calculate predictions for the  $R_{1/2}$ -dependence of galaxy clustering for two classes of empirical models, described in turn below.

#### 3.2.1 Satellite mass loss model

In the first class of models we explore, we suppose that stellar mass  $M_*$  is the statistical regulator of  $R_{1/2}$ , so that galaxy sizes are drawn from a log-normal distribution with 0.2 dex of scatter centered at  $\langle R_{1/2} | M_* \rangle_{\text{median}}$ . To implement this model, for simplicity we tabulate  $\langle R_{1/2} | M_* \rangle_{\text{median}}$  directly from the data, rather than pursue a parametric form (see, e.g., Zhang & Yang 2017).

It is natural to consider the possibility that stellar mass is stripped from satellite galaxies after infall. The basis for our implementation of this phenomenon is the fitting function presented in Smith et al. (2016), which was calibrated by studying stellar mass loss in a suite of high-resolution hydrodynamical simulations. In this model,  $f_*$  quantifies the remaining fraction of stellar mass as a function of  $f_{\text{DM}}$ , the fraction of dark matter mass that remains after subhalo infall:

$$f_* = 1 - \exp(-14.2 f_{\text{DM}}). \quad (1)$$

For  $f_{\text{DM}}$  we use the ratio of present-day subhalo mass divided by the peak mass,  $M_{\text{vir}}/M_{\text{peak}}$ . If we denote the post-stripping stellar mass as  $M'_*$ , then we have  $M'_* \equiv f_* M_*$ , where  $M_*$  is given by the initial application of abundance matching. We then calculate the post-stripping radius by interpolating  $\langle R'_{1/2} | M'_* \rangle$  directly from SDSS data. In this way, we model satellite mass loss and

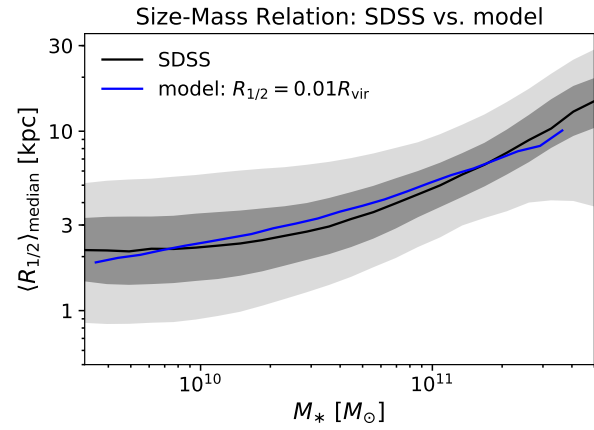


**Figure 3.** The black curve shows the median size-mass relation of SDSS galaxies as measured in Meert et al. (2015). The two gray bands enveloping the black curve show the 50% and 90% percentile regions. The blue curve shows  $R_{\text{vir}}$ -based model in which  $\langle R_{1/2} | R_{\text{vir}} \rangle_{\text{median}} = 0.01 R_{\text{vir}}$ . This figure confirms that a linear relationship between  $R_{\text{vir}}$  and  $R_{1/2}$ , convolved against the nonlinear relationships between  $R_{\text{vir}}$ ,  $M_{\text{halo}}$  and  $M_*$ , predicts the characteristic curvature in the relation  $\langle R_{1/2} | M_* \rangle_{\text{median}}$  over a wide range in mass.

size truncation in a manner that mimics what is seen in hydrodynamical simulations.

#### 3.2.2 $R_{\text{vir}}$ -based model

Motivated by Kravtsov (2013), we additionally explore a model in which  $R_{1/2}$  is linearly proportional to halo virial radius:<sup>4</sup>

$$R_{1/2} = 0.01 R_{\text{vir}}. \quad (2)$$

For the virial radius of halos and subhalos, we use  $R_{\text{Mpeak}}$ : the value of  $R_{\text{vir}}$  in physical units of kpc measured at the time of peak subhalo mass. The relationship between  $R_{\text{Mpeak}}$  and  $M_{\text{peak}}$  is given by

$$M_{\text{peak}} \equiv \frac{4\pi}{3} R_{\text{Mpeak}}^3 \Delta_{\text{vir}}(z_{\text{Mpeak}}) \rho_{\text{m}}(z_{\text{Mpeak}}), \quad (3)$$

where for  $\Delta_{\text{vir}}(z_{\text{Mpeak}})$  we use the fitting function to the “virial” definition used in Bryan & Norman (1998). For the model we refer to as the “ $R_{\text{vir}}$ -based model”, we add uncorrelated log-normal scatter of  $\sigma_{R_{1/2}} = 0.2$  dex to generate a Monte Carlo realization of the model population.

## 4 RESULTS

### 4.1 Size-Mass Scaling Relation

In Figure 3 we show the scaling of galaxy size  $R_{1/2}$  with  $M_*$ . The black curve enveloped by the gray bands shows

<sup>4</sup> We note that the normalization factor in Kravtsov (2013) is 0.0125, where as our normalization is 0.01. The difference derives from the choice of halo radius definition: Bryan & Norman (1998) in the present work, compared to the 200c definition used in Kravtsov (2013).

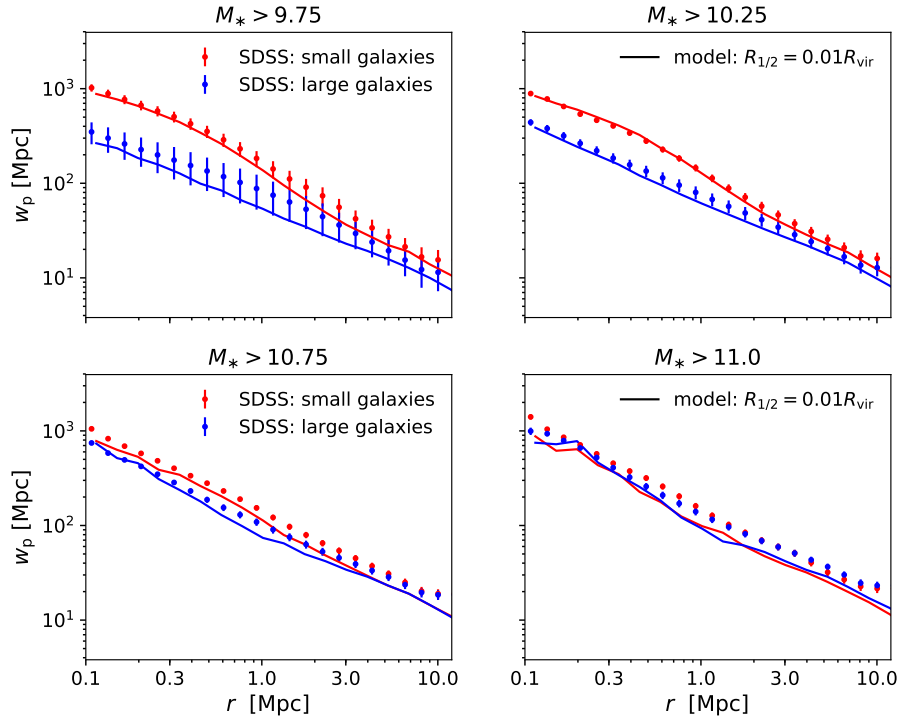


**Figure 4.**  $R_{1/2}$ –dependence of galaxy clustering. Red and blue points with error bars show our SDSS measurements of the clustering of small and large galaxies, respectively. For each volume-limited sample of  $M_*$ –complete galaxies, the small and large subsamples have identical stellar mass functions, as shown in Figure 1. Small galaxies cluster much more strongly relative to large galaxies of the same stellar mass. Solid curves show the clustering predictions of the  $R_{\text{vir}}$ –based model described in §3.2.2. The  $R_{\text{vir}}$ –based model inherits the shortcoming of ordinary abundance matching at  $M_* \gtrsim 10^{10.75} M_\odot$ , although the model faithfully captures the *relative* clustering of small vs. large galaxies, as shown in Figure 5.

the scaling relation for SDSS galaxies, while the blue curve shows the median relation  $\langle R_{1/2} | M_* \rangle_{\text{median}}$  implied by the  $R_{\text{vir}}$ –based model described in §3.2.2. This figure shows that models in which  $R_{1/2} \propto R_{\text{vir}}$  can naturally give rise to the characteristic curvature in the  $R_{1/2} - M_*$  relation, confirming the results in Kravtsov (2013) in a forward modeling context.

## 4.2 Size-Dependent Clustering Measurements

In Figure 4, we present new measurements of the  $R_{1/2}$ –dependence of projected galaxy clustering,  $w_p(r_p)$ . We measure  $w_p(r_p)$  separately for large and small subsamples for four different  $M_*$  thresholds,  $M_* > 10^{9.75} M_\odot$ ,  $M_* > 10^{10.25} M_\odot$ ,  $M_* > 10^{10.75} M_\odot$ , and  $M_* > 10^{11} M_\odot$ . For each threshold, we split the galaxies into “large” and “small” subsamples; as described in §2.1 and illustrated in Figure 1, our size-based selection is defined so that the subsamples have identical stellar mass functions. Red points with jackknife-estimated error bars show SDSS measurements of  $w_p(r_p)$  for small galaxy samples, blue points show the same for large galaxies. Solid curves show  $w_p$  as predicted by the  $R_{\text{vir}}$ –based model described in §3.2.2.

The salient feature of these clustering measurements is that small galaxies cluster more strongly than large galaxies of the same stellar mass. This feature also holds true for galaxies predicted by the  $R_{\text{vir}}$ –based model.

This result may be surprising, since  $R_{1/2} \propto R_{\text{vir}}$ , halo mass  $R_{\text{vir}} \propto M_{\text{halo}}^{1/3}$ , and clustering strength increases with  $M_{\text{vir}}$ . Based on this simple argument, one would expect that large galaxies would be the more strongly clustered. We provide a resolution to this conundrum in §5.1; before doing so, we first examine the clustering test of the  $R_{\text{vir}}$ –based model in more detail.

As shown in Figure 2, the abundance matching prediction for  $w_p(r_p)$  exhibits tension with SDSS observations at the 10 – 20% level, particularly for  $M_* \gtrsim 10^{10.75} M_\odot$ . This tension is inherited by our  $R_{\text{vir}}$ –based model for size, which is the subject of this work, and so we wish to compare our size models to data in such a way that minimizes the role played by the underlying stellar-to-halo-mass relation. We accomplish this using the  $R_{1/2}$  clustering ratios, described below.

For each volume-limited  $M_*$ –threshold sample, we additionally measure  $w_p(r_p)$  *without* splitting on size, giving us measurements  $w_p^{\text{all}}$ ,  $w_p^{\text{large}}$ , and  $w_p^{\text{small}}$  for each threshold sample. This allows us to compute the ratio  $(w_p^{\text{large}} - w_p^{\text{small}})/w_p^{\text{all}}$ , which we refer to as the  $R_{1/2}$  clustering ratio, denoted as  $\delta_{R_{1/2}}(w_p)$ . For example, a clustering ratio of  $-0.5$  corresponds to small galaxies being 50% more strongly clustered than large galaxies of the same stellar mass. These ratios are the measurements appearing on the y-axis in each panel of Figure 5.

The points and curves in Figure 5 are all negative: small galaxies cluster more strongly relative to large.

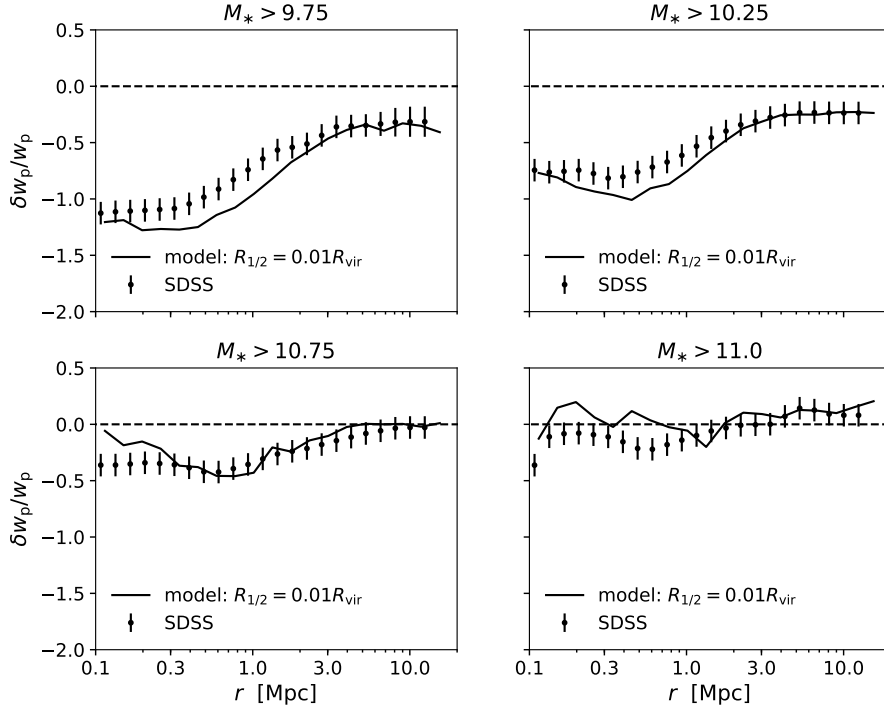


**Figure 5.**  $R_{1/2}$ -dependence of galaxy clustering: clustering ratios. Closely related to Figure 4, the y-axes show *clustering strength ratios*, defined as  $(w_p^{\text{large}} - w_p^{\text{small}})/w_p^{\text{all}}$ . Thus a y-axis value of  $-0.5$  corresponds to small galaxies being 50% more strongly clustered than large galaxies of the same stellar mass. Solid curves show the clustering ratio predictions of the  $R_{\text{vir}}$ -based model described in §3.2.2. Normalizing the measurements and predictions by  $w_p^{\text{all}}$  scales away the shortcoming of ordinary abundance matching at high stellar mass (see Figure 2), highlighting the successful prediction of the  $R_{\text{vir}}$ -based model for the  $R_{1/2}$ -dependence of galaxy clustering.

This presentation of the measurement makes plain that the underlying signal of  $R_{1/2}$ -dependent clustering is strongest for samples with smaller stellar mass; as  $M_*$  increases, the signal weakens and nearly vanishes for  $M_* \gtrsim 10^{11} M_\odot$ . Strikingly, the  $R_{\text{vir}}$ -based model exhibits this  $M_*$ -dependent behavior, as well as the scale-dependence of the observed clustering signal at each  $M_*$ . As described in §5.1 below, we attribute the success of this prediction to the relative sizes of central vs. satellite galaxies.

#### 4.3 Testing the Impact of Satellite Mass Loss

The green curves in Figure 6 test the clustering predictions of the model described in §3.2.1 *before* applying the satellite mass loss prescription. Thus the green curves pertain to a model where  $R_{1/2}$  is a purely random log-normal distribution centered at  $\langle R_{1/2} | M_* \rangle_{\text{median}}$ . By construction, this model predicts no dependence at all of galaxy clustering upon  $R_{1/2}$  at fixed  $M_*$ , simply because the scatter of  $R_{1/2}$  about  $\langle R_{1/2} | M_* \rangle_{\text{median}}$  is uncorrelated with any other property. The application of satellite mass loss introduces correlations in the scatter: after mass loss, satellites have smaller sizes than centrals of the same  $M_*$  due to post-infall stripping.

As shown by the purple curves in Figure 6, satellite mass loss impacts  $R_{1/2}$ -dependent clustering in the expected manner. The “small” galaxy population has a

higher satellite fraction due to satellites being smaller than centrals of the same  $M_*$ , and so in this model small galaxies cluster more strongly relative to large. However, the magnitude of the effect is evidently not strong enough to produce clustering predictions that are consistent with SDSS. Evidently it is difficult to strip enough mass from satellites so that the  $R_{1/2}$ -dependent clustering is in agreement with observations. As we argue in §5, this supports the conclusion that the relative difference between central and satellite size is at least partially in place at the time of satellite infall.

#### 4.4 The Role of Morphology and Color

In this section we take a preliminary look at how galaxy clustering exhibits simultaneous dependence upon broadband color, morphology, and size. Beginning from the  $M_* > 10^{10.25} M_\odot$  sample used above, we first divide the sample into “red” and “blue” subsamples according to a  $g - r = 0.65$  cut, the rough location of the trough of the green valley for this stellar mass. For each color-selected subsample, we separately measure  $\langle R_{1/2} | M_*; \text{red} \rangle_{\text{median}}$  and  $\langle R_{1/2} | M_*; \text{blue} \rangle_{\text{median}}$ , and use these median size values to split each subsample into two.

In the top left panel of Figure 7 we show the clustering of large vs. small red galaxies; in the top right panel we show the same for blue galaxies. For each color-selected sample, large galaxies are slightly more strongly

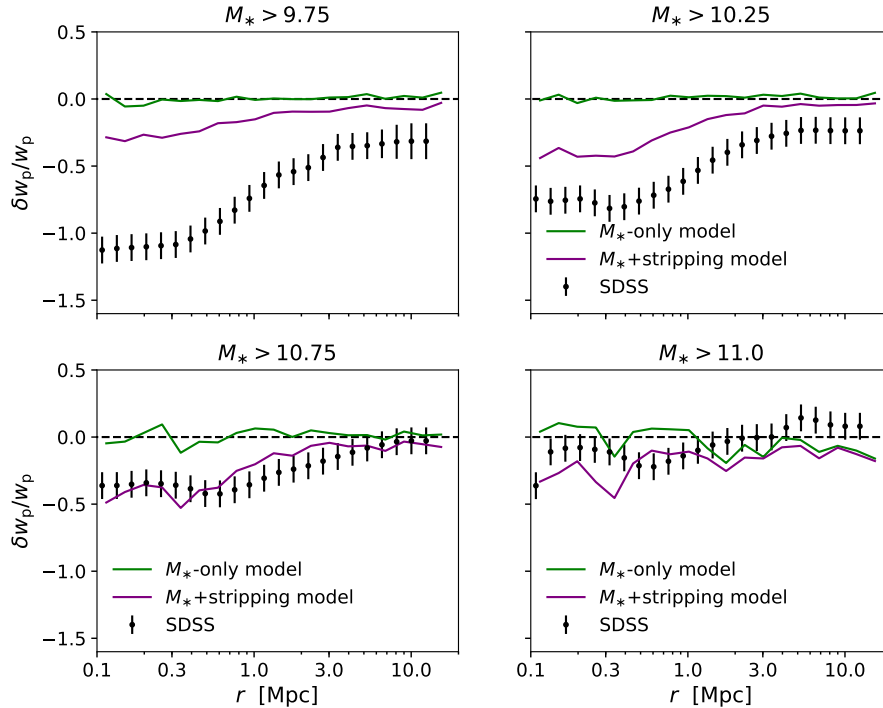


**Figure 6. The subdominant role of tidal stripping.** In all panels, the axes and points with error bars are the same as in Figure 5. The solid green curves show the prediction of the satellite mass loss model, which is in gross tension with the data due to satellites having the same size as centrals of the same mass. The solid purple curves show results for a model in which satellites lose mass after infall in a manner similar to what is seen in high-resolution hydrodynamical simulations, as described in §3.2.1. This produces satellites that are smaller than centrals, but the effect is too mild to correctly capture the observed clustering. Evidently, satellite-specific mass stripping plays a sub-dominant role in setting the relative size of centrals and satellites.

clustered relative to small galaxies. Comparing the top panels of Figure 7 to the upper right panel of Figure 4 shows the dramatic impact of galaxy color selection upon  $R_{1/2}$ -dependent clustering. For  $M_*$ -complete samples, small galaxies cluster much stronger than large galaxies; for color-selected samples, the reverse is true, and the magnitude of the effect weakens considerably.

The bottom panels of Figure 7 show results that are analogous to the top panels, but instead using of  $g-r$  color, we first divide the  $M_* > 10^{10.25} M_\odot$  sample into “bulge-dominated” and “disk-dominated” sequences according to  $B/T$ , the fraction of  $r$ -band flux coming from the bulge component of the 2d light profile measurements in the Meert et al. (2015) catalog. We define a galaxy as bulge-dominated if  $B/T < 0.25$ , and disk-dominated if  $B/T > 0.75$ . We separately split the disk-dominated and bulge-dominated subsample into two based on the median size  $\langle R_{1/2} | M_*, B/T \rangle_{\text{median}}$  appropriate for each subsample. The bottom left panel of Figure 7 compares the clustering of small vs. large disk-dominated galaxies; the bottom right panel shows the same comparison for bulge-dominated galaxies.

The contrast between the two bottom panels is stark. The clustering of large vs. small bulge-dominated galaxies has almost no dependence upon  $R_{1/2}$ . On the other hand, for disk-dominated galaxies, small galaxies are much more strongly clustered, and the effect is strong. In fact, comparing the bottom left panel of Figure 7 to the top right panel of Figure 4, we see that  $R_{1/2}$ -dependent

clustering is quite similar between disk-dominated galaxies and  $M_*$ -threshold samples. We discuss a halo model interpretation of these trends in §5.

## 5 A UNIFIED INTERPRETATION OF $R_{1/2}$ -DEPENDENT CLUSTERING

The clustering measurements shown in the previous section present (at least) two intriguing puzzles. First, the modeling assumption  $R_{1/2} \propto R_{\text{vir}}$  predicts size-dependent galaxy clustering that is in quite good agreement with observations, particularly considering the simplicity of the model. Yet, small galaxies cluster more strongly relative to large, which seems at odds with naive expectations based on halo mass, since  $R_{\text{vir}} \propto M_{\text{vir}}$ . Second, there appears to be a highly non-trivial dependence of  $R_{1/2}$ -dependent clustering upon whether or not the galaxy sample has been selected by color or morphology. We propose a simple and unified solution to both puzzles in §5.1, and discuss the broader implications of our interpretation in §5.2.

### 5.1 The Relative Size of Centrals vs. Satellites

A straightforward resolution to the first puzzle is shown in Figure 9, which compares the  $R_{1/2}$  distributions of central, satellite, and splashback galaxies with the same



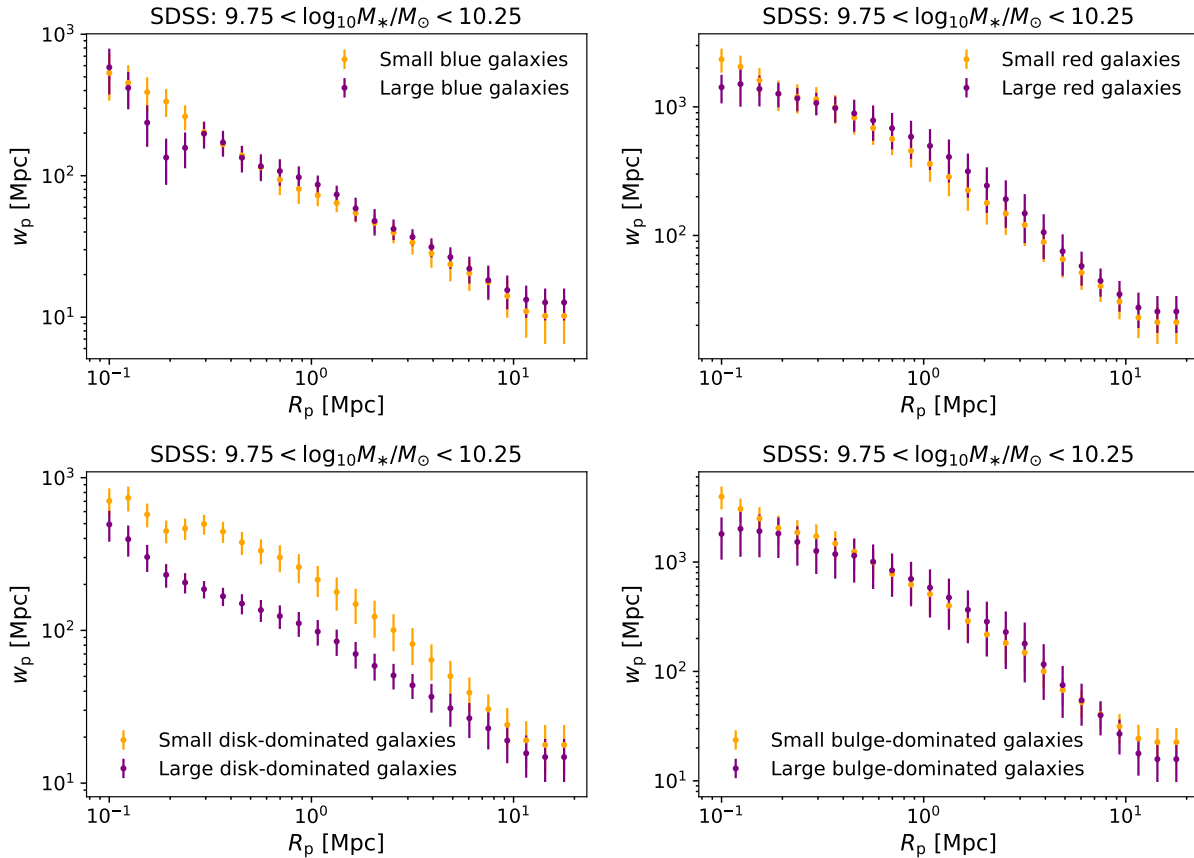


**Figure 7. Distinct  $R_{1/2}$ –dependence of clustering for color- or morphology-selected galaxy samples.** All panels show the clustering of galaxies in the same bin of stellar mass:  $10^{9.75} < M_*/M_\odot < 10^{10.25}$ . In the *upper left* panel, we first select blue galaxies based on  $g - r < 0.6$ , and subsequently compute  $\langle R_{1/2}|M_* \rangle_{\text{median}}$  of the *color-selected* sample. This results in identical stellar mass function for large and small blue galaxy samples, in analogy to the left panel of Figure 1. The *upper right* panel shows results of the same procedure for “red” galaxies, defined by  $g - r > 0.6$ . The top two panels show that for color-selected samples, the magnitude of the  $R_{1/2}$ –dependence of clustering is dramatically reduced, and changes sign, relative to  $M_*$ –complete samples. Using the Meert et al. (2015) measurements of the disk/bulge decomposition of the 2d  $r$ –band luminosity profile  $L_r$ , the bottom left panel shows analogous results for disk-dominated galaxies defined by  $L_r^{\text{bulge}} < L_r^{\text{tot}}/4$ ; the bottom right panel shows results for bulge-dominated galaxies defined by  $L_r^{\text{disk}} < L_r^{\text{tot}}/4$ .

halo mass  $M_{\text{halo}} \equiv M_{\text{peak}} \approx 10^{12} M_\odot$ . A “splashback central” is defined as a present-day central that used to be a satellite, i.e., its main progenitor halo passed inside the virial radius of a larger halo at some point in its past history. On the other hand, we define a “true central” as a galaxy that has never been a satellite.

In the  $R_{\text{vir}}$ –based model, satellite and splashback galaxies are smaller than centrals of the same halo mass due to the physical size of their halo being smaller at earlier times  $z_{M_{\text{peak}}}$ . There are two distinct reasons why this feature results in small galaxies being more strongly clustered relative to larger galaxies of the same mass. First and foremost, satellite galaxies statistically occupy higher mass host halos that are more strongly clustered. So in models where satellites are smaller than centrals, at fixed  $M_*$  the “small” subsample will naturally have a higher satellite fraction, boosting the clustering of small galaxies relative to large of the same stellar mass. Second, at fixed mass, halos of  $L_*$  galaxies that form earlier are more strongly clustered, a phenomenon commonly known as *halo assembly bias*. Splashback halos are typ-

ically earlier-forming than true centrals, and so models where splashback halos host smaller-than-average galaxies will naturally predict smaller galaxies being the more strongly clustered.

We can also understand the  $M_*$ –dependence of Figure 5 in term of the relative sizes of centrals vs. satellites. The satellite fraction  $F_{\text{sat}}(M_*)$  decreases as  $M_*$  increases (e.g., Guo et al. 2011; Reddick et al. 2013). As  $F_{\text{sat}}$  decreases, there are fewer satellites available to preferentially weight the subsample of smaller galaxies. Thus models where  $R_{1/2}$ –dependent clustering is driven by satellite vs. central size naturally predict the observed  $M_*$ –dependence of the signal, without introducing any explicitly  $M_*$ –dependent ingredients in the size model.

Upon first glance, the  $R_{1/2}$ –dependence of color- and morphology-selected samples shown in Figure 7 appear to be driven by different principles, since the trends substantially weaken and change sign. However, even very simple models based entirely on central vs. satellite size differences can give rise to this behavior. For example, it is well known that satellites are redder than centrals

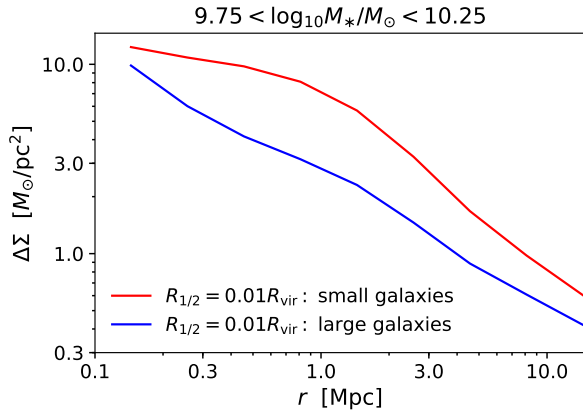


**Figure 8. Prediction for  $R_{1/2}$ -dependence of galaxy lensing.** Using the  $R_{\text{vir}}$ -based model described in §3.2.2, we make predictions for as-yet-unseen measurements of the  $R_{1/2}$ -dependence of galaxy lensing of  $M_*$ -complete samples. To date, the  $R_{1/2}$ -dependence of  $\Delta\Sigma$  has only been measured for color-selected samples (Charlton et al. 2017), in which the reverse is true: for both blue and red samples,  $\Delta\Sigma$  of small galaxies is (weakly) suppressed relative to large galaxies. As a generic consequence of satellites being smaller than centrals of the same mass, we predict that the analogous measurement for  $M_*$ -complete samples will show  $\Delta\Sigma$  of small galaxies to be much stronger relative to large galaxies of the same stellar mass.

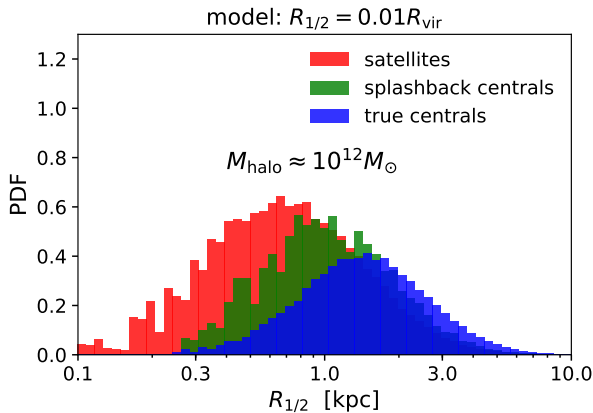


**Figure 9. Relative sizes of centrals and satellites.** In a narrow bin of halo mass  $M_{\text{halo}} \equiv M_{\text{peak}} \approx 10^{12} M_{\odot}$ , we show the distribution of model galaxy sizes for different subpopulations galaxies, as predicted by the  $R_{\text{vir}}$ -based model. The red histogram shows the sizes of satellites; the blue histogram shows host halos that have never passed inside the virial radius of a larger halo (“true centrals”); the green histogram host halos that were subhalos inside a larger at some point in their past history (“splashback centrals”). In the  $R_{\text{vir}}$ -based model, galaxy size is set by the *physical* size of the virial radius at the time the halo attains its peak mass, naturally resulting in smaller sizes for satellites and splashback centrals relative to true centrals of the same  $M_{\text{halo}}$ .

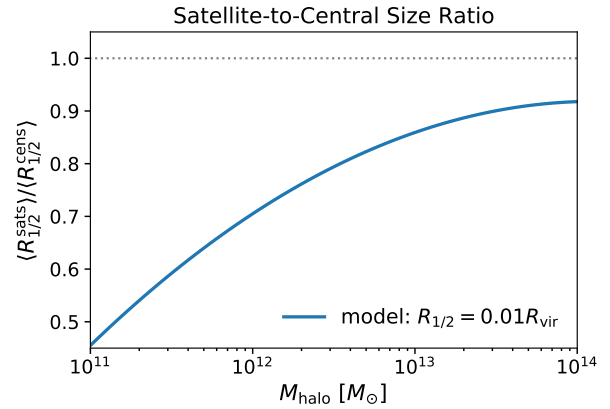


**Figure 10. Scaling relation for hydro sims and SAMs.** As a function of subhalo mass  $M_{\text{halo}} = M_{\text{peak}}$ , we show the ratio of mean satellite-to-central size predicted by the  $R_{\text{vir}}$ -based model. This scaling relation should be a useful guideline for more fine-grained physical models of galaxy size that wish to reproduce the observed  $R_{1/2}$ -dependence of galaxy clustering.

(e.g., van den Bosch et al. 2008); accordingly, red galaxies cluster much stronger relative to blue (Zehavi et al. 2011). Pre-selecting galaxy samples by color will thus significantly weaken the dynamic range of  $F_{\text{sat}}$  within each color-selected subsample. This reduction in the role of satellites could be sufficient for the  $R_{1/2} \propto R_{\text{vir}} \propto M_{\text{halo}}$  of *central* galaxies to become the dominant effect, which would result in the mild, reversed trend seen in the top panels of Figure 7. The same satellite-driven mechanism could be at work for the case of morphology pre-selection (as in the morphology models developed in Skibba et al. 2009), except that for disk-dominated systems, there would need to be a larger residual correlation with satellite designation relative to blue-selected samples (which is, in fact, exactly the trend reported in Weinmann et al. 2009).

While we consider such an explanation plausible, a conclusive determination of the principles underlying the clustering trends shown in Figure 7 requires proper forward modeling of morphology and color jointly with galaxy size. Such an effort is beyond the scope, but well-motivated, by the present work. See Section 5.2 for further discussion.

## 5.2 Broader Implications

Physical explanations for differences between the sizes of centrals and satellites fall into two categories, depending on whether or not the processes involved are post-infall and satellite-specific. In the satellite mass loss model, satellites evolve exactly as centrals prior to the time of infall; this model assumes that *all* satellite size truncation occurs after the time of infall. The  $R_{\text{vir}}$ -based model assumes the opposite: namely that the size of *all* galaxies is statistically set by the  $R_{M_{\text{peak}}}$ , the physical size of the virial radius at the time at which  $M_{\text{halo}}$  stops growing. This assumption is the natural extension of the abundance matching approximation that stellar



mass largely stops growing at this time (including in-situ and ex-situ growth). The halos of typical satellites reach  $M_{\text{peak}}$  far outside the virial radius of their ultimate host halo (Behroozi et al. 2014), and so in the  $R_{\text{vir}}$ -based model the size differences between satellites and centrals is largely in place prior to the time of satellite infall.

The clustering ratios in Figure 6 show that the impact of physically motivated levels of satellite mass loss likely cannot explain the  $R_{1/2}$ -dependent clustering seen in SDSS. As an additional test, we reach the same conclusion when implementing an even more extreme  $M_*$ -stripping model in which stellar mass loss is linearly proportional to halo mass loss (Watson et al. 2012, Model 1). The success of the  $R_{\text{vir}}$ -based model, together with the failure of the satellite mass loss model, suggests that the relative size of central and satellite galaxies is largely driven by the pre-infall evolution of the satellite.

The broad features of the  $w_p(r_p)$  measurements shown in Figure 7 give insight into the characteristics that should be exhibited by any model for the relationship between  $B/T$  and  $R_{1/2}$ . First, the bottom right panel of Figure 7 indicates that the size of the bulge has only a tenuous connection to the properties of its parent dark matter halo.<sup>5</sup> Second, for disk-dominated galaxies, the observed  $R_{1/2}$ -dependent clustering suggests that at fixed  $M_*$ , the size of the disk is strongly correlated with whether or not the galaxy is a satellite. These findings imply that bulge prominence is intimately connected with the quenching of star-formation, but that there is wide variation in star-formation histories amongst disk-dominated galaxies, in agreement with numerous previous findings (see, e.g., Woo et al. 2015; Font et al. 2017).

Recent progress has substantially improved capabilities for the richness of the predictions of empirical galaxy-halo models (Becker 2015; Cohn 2017; Moster et al. 2017). This new class of models has accomplished this by empirically modeling star-formation rate, and then integrating SFR along each halo’s history to differentially build up stellar mass. In ongoing follow-up work, we are currently extending this new class of models to differentially build up the disk and bulge across cosmic time using computationally efficient empirical modeling methods. In addition to treating the multi-dimensional nature of the problem, this will allow us to use data at higher redshift in a self-consistent manner.

## 6 RELATION TO PREVIOUS WORK

Numerous previous analyses have employed the Yang et al. (2005) group catalog to “directly” study the relationship between galaxy mass, size, and environment. For example, by treating observed groups as genuine dark matter halos, several analyses have found that the  $M_* - R_{1/2}$  relation of early-type galaxies exhibits weak, if any, environmental dependence (Weinmann et al.

2009; Huertas-Company et al. 2013; Shankar et al. 2014). Meanwhile, Weinmann et al. (2009) additionally find that for late-type galaxies, there is a strong correlation between disk size and central/satellite designation. Qualitatively, our clustering measurements shown in Figure 7 are in good agreement with these findings: once galaxies have been morphology-selected, only the clustering of disk shows significant dependence upon  $R_{1/2}$ . Our clustering results are also consistent with the disk model presented in Dutton et al. (2007, 2011), which predicts that at fixed stellar mass, there is weak, positive correlation between disk size and halo mass.

As discussed in Spindler & Wake (2017), it is entirely possible that size differences between centrals and satellites of the same mass can be accounted for by mutual covariance with an additional variable such as star formation rate or morphological type (see also Lilly & Carollo 2016, for an explicit demonstration of this scenario). In particular, suppose that centrals and satellites of the same mass have different early-type fractions as indicated in Weinmann et al. (2006), and that early- and late-type galaxies exhibit universal, but distinct,  $M_* - R_{1/2}$  relations. In such a case, centrals would be larger than satellites of the same mass, even though *early-type centrals* would have the same sizes as *early-type satellites*. This scenario could also explain the sign-change and weakening of  $R_{1/2}$ -dependent clustering measurements in the present work.

The  $R_{1/2}$ -dependence of galaxy lensing has recently been measured using CFHTLenS observations (Heymans et al. 2012; Erben et al. 2013). For both red- and blue-sequence galaxies, it was found in Charlton et al. (2017) that the lensing signal,  $\Delta\Sigma$ , of large galaxies is slightly stronger relative to smaller galaxies. This result is in good agreement with the clustering measurements in the top panels of Figure 7, which show the same trend. To date, the  $R_{1/2}$ -dependence of  $\Delta\Sigma$  not yet been measured for  $M_*$ -complete samples. We show predictions of the  $R_{\text{vir}}$ -based model for future measurements of this signal in Figure 8. The halo model explanation for this trend is the same as for  $w_p$ : satellites occupy higher mass host halos relative to centrals of the same stellar mass, boosting  $\Delta\Sigma$  for small relative to large galaxy samples.

Our methodology is closely aligned with Somerville et al. (2017), who studied the empirical modeling features that are necessary to recover the tight scatter in the observed  $\langle R_{1/2} | M_* \rangle$  relation. By building models where  $R_{1/2}$  is set by halo spin  $\lambda_{\text{halo}}$ , the authors in Somerville et al. (2017) found that the level of intrinsic scatter about  $\langle \lambda_{\text{halo}} | M_{\text{halo}} \rangle$  in dark matter halos is at least as large as the scatter about  $\langle R_{1/2} | M_* \rangle$  seen in observed galaxies. In our approach, the level of scatter is simply a modeling parameter whose fiducial value was motivated by Somerville et al. (2017). In ongoing follow-up work discussed in §7, we will systematically test the large-scale structure implications of the assumption that  $\lambda_{\text{halo}} \propto R_{1/2}^{\text{disk}}$  using forward-modeling methods analogous to those advocated for in Somerville et al. (2017) and employed here.

<sup>5</sup> Strictly speaking, the size of the bulge could in principle be closely connected to any number of dark matter halo properties, so long as those halo properties do not significantly impact two-point clustering.

## 7 FUTURE DIRECTIONS FOR EMPIRICAL MODELING OF GALAXY SIZE AND MORPHOLOGY

The scope of this work is to serve as a pilot study in which we identify the chief ingredients that can influence the  $R_{1/2}$ -dependence of galaxy clustering. While our results suggest that satellite evolution *prior* to infall drives the correct relative size of centrals vs. satellites, our implementation cannot be correct in quantitative detail: the clustering ratios of this model shown in Figure 5 only roughly agree with SDSS. For present purposes, we have chosen to focus on exploring bracketing cases of qualitative ingredients, rather than fine-tuning the model.

Since the clustering signal is strongly influenced by differences between centrals and satellites, then the satellite fraction  $F_{\text{sat}}(M_*)$  plays an important role in  $R_{1/2}$ -dependent clustering. For *fixed* scaling relations  $\langle R_{1/2}^{\text{cens}} | M_{\text{halo}} \rangle_{\text{median}}$  and  $\langle R_{1/2}^{\text{sats}} | M_{\text{halo}} \rangle_{\text{median}}$ , models with different satellite fractions will exhibit different  $R_{1/2}$ -clustering ratios because  $F_{\text{sat}}(M_*)$  controls the relative weighting of the two populations. An explicit demonstration of this point appears in the Appendix, which repeats the analyses in the main body of the text, but for a subhalo catalog with no orphan correction.

On the one hand, this degeneracy with the satellite fraction is unfortunate, because it means galaxy size does not leave a pure and unique signature on  $R_{1/2}$ -clustering ratios. However, this can also be viewed as an opportunity to extract tighter constraints on  $F_{\text{sat}}(M_*)$ , which are sorely needed to discriminate between competing models (Watson & Conroy 2013). Traditional galaxy clustering is already being used to validate and/or fit models of the stellar-to-halo-mass relation (e.g., Leauthaud et al. 2012; Moster et al. 2013; Behroozi et al. 2013; Lehmann et al. 2017). Based on our results, we advocate that empirical models for  $\langle M_* | M_{\text{halo}} \rangle$  be supplemented with additional model ingredients for  $\langle R_{1/2} | M_* \rangle_{\text{median}}$ , and that the parameters of the composite model be *jointly* constrained by measurements of the stellar mass function,  $M_*$ -dependent clustering, and  $R_{1/2}$ -dependent clustering.

Figure 10 shows that the satellites in  $M_{\text{halo}} \approx 10^{12} M_{\odot}$  halos can be as large as  $\lesssim 40 - 50\%$  smaller than their central galaxy counterparts. Since the satellite fraction varies quite significantly with morphology and/or color, we have demonstrated that it is entirely plausible that most of the observed environmental trends of galaxy size can be understood simply in terms of central vs. satellite size differences. While it remains to be seen whether this explanation ends up comprising the whole story, one thing is now clear: it is simply not possible to reliably analyze environmental trends of galaxy  $R_{1/2}$  without properly accounting for satellites. Because of the large systematics that are common in contemporary group-finding methods (Campbell et al. 2015), we consider forward modeling methods to be a requisite for meaningful continued progress on this topic.<sup>6</sup>

<sup>6</sup> We note that group-finders may play an important role in future analyses of galaxy size. However, it was shown in Campbell et al. (2015) that treating observed groups as if they were

## 8 CONCLUSIONS

We have presented new measurements of the dependence of galaxy clustering upon galaxy size, and used **Halotools** to identify the basic ingredients that influence the signal. We conclude with a brief summary of our primary findings:

(i) Small galaxies cluster more strongly than large galaxies of the same stellar mass. Differences between the clustering of small and large galaxies increase on small scales  $R \lesssim 1\text{Mpc}$ , and decrease with stellar mass.

(ii) The most important ingredient influencing this signal is the relative size of central and satellite galaxies. The magnitude, scale-dependence, and  $M_*$ -dependence of  $R_{1/2}$ -dependent clustering provides strong evidence that satellite galaxies are smaller than central galaxies of the same halo mass.

(iii) A simple empirical model in which  $R_{1/2}$  is set by halo  $R_{\text{vir}}$  at the time of peak halo mass exhibits a clustering signal that is strikingly similar to that seen in SDSS.

(iv) Models in which  $R_{1/2}$  is regulated by  $M_*$ , rather than  $M_{\text{halo}}$ , are grossly discrepant with the observed clustering signal, even when accounting for satellite mass stripping.

(v) Taken together, our findings indicate that satellite-specific processes play a sub-dominant role in setting the relative size of centrals and satellites, which instead appears to be largely predetermined at the time of satellite infall.

Our results can be treated as a boundary condition for more complex and fine-grained models of galaxy size, such as semi-analytic models and hydrodynamical simulations. For convenience, Figure 10 provides a simple summary statistic that can be used as a diagnostic for calibrating alternative modeling efforts. We view the present work as a pilot study that motivates a Bayesian inference program to tightly constrain the galaxy size-halo connection with forward modeling techniques, in direct analogy to the literature on the stellar-to-halo-mass relation. Our publicly available python code provides a simple means for cosmological surveys to generate synthetic galaxy populations with realistic sizes across the cosmic web.

## ACKNOWLEDGMENTS

APH thanks John Baker for the *Toejam & Earl* soundtrack. Thanks also to Frank van den Bosch, Andrew Zentner, Doug Watson, and Risa Wechsler for thoughtful feedback at various stages of the development of this work, and to Faustin Carter and Sebastian Bocquet for sharing their matplotlib expertise.

correctly identified dark matter halos can lead to entirely unreliable conclusions. The robust method to extract information from galaxy group catalogs is instead to generate a Monte Carlo realization of a forward model, and then run the same group-finding algorithm on the mock as was run on the data, enabling a proper apples-to-apples comparison.

We thank the *Astropy* developers for the package-template (Astropy Collaboration et al. 2013), and *NumPy* (Van Der Walt et al. 2011), *SciPy* (Jones et al. 2016), *IPython*, *Matplotlib*, and *GitHub* for their extremely useful free software.

This research was supported in part by the National Science Foundation under Grant No. NSF PHY11-25915. Work done at Argonne National Laboratory was supported under the DOE contract DE-AC02-06CH11357.

## REFERENCES

- Ahn C. P., Alexandroff R., Allende Prieto C., Anders F., Anderson S. F., Anderton T., Andrews B. H., Aubourg É., Bailey S., Bastien F. A., et al. 2014, *ApJS*, 211, 17
- Astropy Collaboration Robitaille T. P., Tollerud E. J., Greenfield P., Droettboom M., Bray E., Aldcroft T., et al., 2013, *AAP*, 558, A33
- Becker M. R., 2015, *ArXiv:1507.03605*
- Behroozi P. S., Conroy C., Wechsler R. H., 2010, *ApJ*, 717, 379
- Behroozi P. S., Wechsler R. H., Conroy C., 2013, *ApJ*, 770, 57
- Behroozi P. S., Wechsler R. H., Lu Y., Hahn O., Busha M. T., Klypin A., Primack J. R., 2014, *ApJ*, 787, 156
- Behroozi P. S., Wechsler R. H., Wu H.-Y., 2013, *ApJ*, 762, 109
- Behroozi P. S., Wechsler R. H., Wu H.-Y., Busha M. T., Klypin A. A., Primack J. R., 2013, *ApJ*, 763, 18
- Behroozi P. S., Zhu G., Ferguson H. C., Hearin A. P., Lotz J., Silk J., Kassin S., Lu Y., Croton D., Somerville R. S., Watson D. F., 2015, *MNRAS*, 450, 1546
- Bernardi M., Meert A., Sheth R. K., Vikram V., Huertas-Company M., Mei S., Shankar F., 2013, *MNRAS*, 436, 697
- Bernardi M., Meert A., Vikram V., Huertas-Company M., Mei S., Shankar F., Sheth R. K., 2014, *MNRAS*, 443, 874
- Bottrell C., Torrey P., Simard L., Ellison S. L., 2017, *MNRAS*, 467, 2879
- Brinchmann J., Charlot S., White S. D. M., Tremonti C., Kauffmann G., Heckman T., Brinkmann J., 2004, *MNRAS*, 351, 1151
- Bryan G. L., Norman M. L., 1998, *ApJ*, 495, 80
- Cacciato M., van den Bosch F. C., More S., Mo H., Yang X., 2013, *MNRAS*, 430, 767
- Campbell D., van den Bosch F. C., Hearin A., Padmanabhan N., Berlind A., Mo H. J., Tinker J., Yang X., 2015, *MNRAS*, 452, 444
- Campbell D., van den Bosch F. C., Padmanabhan N., Mao Y.-Y., Zentner A. R., Lange J. U., Jiang F., Villarreal A., 2017, *ArXiv:1705.06347*
- Charlton P. J. L., Hudson M. J., Balogh M. L., Khatri S., 2017, *MNRAS*, 472, 2367
- Cohn J. D., 2017, *MNRAS*, 466, 2718
- Coil A. L., Newman J. A., Croton D., Cooper M. C., Davis M., Faber S. M., Gerke B. F., Koo D. C., Padmanabhan N., Wechsler R. H., Weiner B. J., 2008, *ApJ*, 672, 153
- Croton D. J., 2013, *PASA*, 30, e052
- Desmond H., Mao Y.-Y., Wechsler R. H., Crain R. A., Schaye J., 2017, *MNRAS*, 471, L11
- Dutton A. A., van den Bosch F. C., Dekel A., Courteau S., 2007, *ApJ*, 654, 27
- Dutton A. A., van den Bosch F. C., Faber S. M., Simard L., Kassin S. A., Koo D. C., Bundy K., Huang J., Weiner B. J., Cooper M. C., Newman J. A., Mozena M., Koekemoer A. M., 2011, *MNRAS*, 410, 1660
- Erben T., Hildebrandt H., Miller L., et al., 2013, *MNRAS*, 433, 2545
- Font A. S., McCarthy I. G., Le Brun A. M. C., Crain R. A., Kelvin L. S., 2017, *ArXiv:1710.00415*
- Guo Q., White S., 2014, *MNRAS*, 437, 3228
- Guo Q., White S., Boylan-Kolchin M., De Lucia G., Kauffmann G., Lemson G., Li C., Springel V., Weinmann S., 2011, *MNRAS*, 413, 101
- Guo Y., McIntosh D. H., Mo H. J., Katz N., Van Den Bosch F. C., Weinberg M., Weinmann S. M., Pasquali A., Yang X., 2009, *MNRAS*, 398, 1129
- Hearin A., Campbell D., Tollerud E., et al., 2016, *ArXiv e-prints*
- Hearin A. P., Watson D. F., 2013, *MNRAS*, 435, 1313
- Heymans C., Van Waerbeke L., Miller L., et al., 2012, *MNRAS*, 427, 146
- Hou J., Lacey C. G., Frenk C. S., 2017, *ArXiv:1708.02950*
- Huang K.-H., Fall S. M., Ferguson H. C., van der Wel A., Grogin N., Koekemoer A., Lee S.-K., Pérez-González P. G., Wuyts S., 2017, *ApJ*, 838, 6
- Huang S., Ho L. C., Peng C. Y., Li Z.-Y., Barth A. J., 2013, *ApJ*, 766, 47
- Huertas-Company M., Mei S., Shankar F., Delaye L., Raichoor A., Covone G., Finoguenov A., Kneib J. P., Le F. O., Povic M., 2013, *MNRAS*, 428, 1715
- Huertas-Company M., Shankar F., Mei S., Bernardi M., Aguerri J. A. L., Meert A., Vikram V., 2013, *ApJ*, 779, 29
- Jiang F., van den Bosch F. C., 2014, *ArXiv e-prints*
- Jones E., Oliphant T., Peterson P., et al., 2001-2016, <http://www.scipy.org>
- Kauffmann G., Heckman T. M., White S. D. M., et al., 2003, *MNRAS*, 341, 33
- Kawamata R., Ishigaki M., Shimasaku K., Oguri M., Ouchi M., 2015, *ApJ*, 804, 103
- Khochfar S., Silk J., 2006, *ApJL*, 648, L21
- Klypin A. A., Trujillo-Gomez S., Primack J., 2011, *ApJ*, 740, 102
- Kravtsov A., Vikhlinin A., Meshcheryakov A., 2014, *ArXiv:1401.7329*
- Kravtsov A. V., 2013, *ApJL*, 764, L31
- Lange R., Driver S. P., Robotham A. S. G., et al., 2015, *MNRAS*, 447, 2603
- Leauthaud A., Tinker J., Bundy K., et al., 2012, *ApJ*, 744, 159
- Lehmann B. V., Mao Y.-Y., Becker M. R., Skillman S. W., Wechsler R. H., 2017, *ApJ*, 834, 37
- Lilly S. J., Carollo C. M., 2016, *ApJ*, 833, 1
- Meert A., Vikram V., Bernardi M., 2013, *MNRAS*, 433, 1344
- Meert A., Vikram V., Bernardi M., 2015, *MNRAS*, 446, 3943
- Moster B. P., Naab T., White S. D. M., 2013, *MNRAS*,

- 428, 3121  
Moster B. P., Naab T., White S. D. M., 2017, ArXiv e-prints  
Moster B. P., Somerville R. S., Maulbetsch C., van den Bosch F. C., Macciò A. V., Naab T., Oser L., 2010, *ApJ* , 710, 903  
Moustakas J., Coil A. L., Aird J., Blanton M. R., Cool R. J., Eisenstein D. J., Mendez A. J., Wong K. C., Zhu G., Arnouts S., 2013, *ApJ* , 767, 50  
Planck Collaboration Ade P. A. R., Aghanim N., Arnaud M., Ashdown M., Aumont J., Baccigalupi C., Banday A. J., Barreiro R. B., Bartlett J. G., et al. 2016, *AAP*, 594, A13  
Reddick R. M., Wechsler R. H., Tinker J. L., Behroozi P. S., 2013, *ApJ* , 771, 30  
Riebe K., Partl A. M., Enke H., Forero-Romero J., Gottlöber S., Klypin A., Lemson G., Prada F., Primack J. R., Steinmetz M., Turchaninov V., 2013, *Astronomische Nachrichten*, 334, 691  
Rodríguez-Puebla A., Behroozi P., Primack J., Klypin A., Lee C., Hellinger D., 2016, *MNRAS* , 462, 893  
Shankar F., Mei S., Huertas-Company M., Moreno J., Fontanot F., Monaco P., Bernardi M., Cattaneo A., Sheth R., Licitra R., Delaye L., Raichoor A., 2014, *MNRAS* , 439, 3189  
Shen S., Mo H. J., White S. D. M., Blanton M. R., Kauffmann G., Voges W., Brinkmann J., Csabai I., 2003, *MNRAS* , 343, 978  
Shibuya T., Ouchi M., Harikane Y., 2015, *ApJS* , 219, 15  
Sinha M., Garrison L., , 2017, Corrfunc: Blazing fast correlation functions on the CPU, Astrophysics Source Code Library  
Skibba R. A., Bamford S. P., Nichol R. C., Lintott C. J., Andreescu D., Edmondson E. M., Murray P., Raddick M. J., Schawinski K., Slosar A., Szalay A. S., Thomas D., Vandenberg J., 2009, *MNRAS* , 399, 966  
Skibba R. A., Coil A. L., Mendez A. J., Blanton M. R., Bray A. D., Cool R. J., Eisenstein D. J., Guo H., Miyaji T., Moustakas J., Zhu G., 2015, *ApJ* , 807, 152  
Smith R., Choi H., Lee J., Rhee J., Sanchez-Janssen R., Yi S. K., 2016, *ApJ* , 833, 109  
Somerville R. S., Behroozi P., Pandya V., et al., 2017, ArXiv e-prints  
Spindler A., Wake D., 2017, *MNRAS* , 468, 333  
Tinker J. L., Leauthaud A., Bundy K., George M. R., Behroozi P., Massey R., Rhodes J., Wechsler R. H., 2013, *ApJ* , 778, 93  
Tinker J. L., Weinberg D. H., Zheng Z., Zehavi I., 2005, *ApJ* , 631, 41  
Trujillo I., Rudnick G., Rix H.-W., Labbé I., Franx M., Daddi E., van Dokkum P. G., Förster Schreiber N. M., Kuijken K., Moorwood A., Röttgering H., van der Wel A., van der Werf P., van Starkenburg L., 2004, *ApJ* , 604, 521  
van den Bosch F. C., Aquino D., Yang X., Mo H. J., Pasquali A., McIntosh D. H., Weinmann S. M., Kang X., 2008, *MNRAS* , 387, 79  
Van Der Walt S., Colbert S. C., Varoquaux G., 2011, ArXiv:1102.1523  
van der Wel A., Franx M., van Dokkum P. G., et al., 2014, *ApJ* , 788, 28  
Vikram V., Wadadekar Y., Kembhavi A. K., Vijayagovindan G. V., 2010, *MNRAS* , 409, 1379  
Wang L., Li C., Kauffmann G., De Lucia G., 2007, *MNRAS* , 377, 1419  
Watson D. F., Berlind A. A., Zentner A. R., 2012, *ApJ* , 754, 90  
Watson D. F., Conroy C., 2013, *ApJ* , 772, 139  
Watson D. F., Hearin A. P., Berlind A. A., Becker M. R., Behroozi P. S., Skibba R. A., Reyes R., Zentner A. R., van den Bosch F. C., 2015, *MNRAS* , 446, 651  
Weinmann S. M., Kauffmann G., van den Bosch F. C., Pasquali A., McIntosh D. H., Mo H., Yang X., Guo Y., 2009, *MNRAS* , 394, 1213  
Weinmann S. M., van den Bosch F. C., Yang X., Mo H. J., 2006, *MNRAS* , 366, 2  
Woo J., Dekel A., Faber S. M., Koo D. C., 2015, *MNRAS* , 448, 237  
Yang X., Mo H. J., Jing Y. P., van den Bosch F. C., 2005, *MNRAS* , 358, 217  
Zehavi I., Zheng Z., Weinberg D. H., et al., 2011, *ApJ* , 736, 59  
Zhang Y., Yang X., 2017, ArXiv e-prints

## APPENDIX: TREATMENT OF DISRUPTED SUBHALOS

We use an extension of **Consistent Trees** that models the evolution of subhalos after disruption. The phase space evolution of disrupted subhalos is approximated by following a point mass evolving in the host halo potential according to the orbital parameters of the subhalo at the time of disruption; the evolution of subhalo mass and circular velocity is approximated using the semi-analytic model presented in Jiang & van den Bosch (2014). We then use the **orphans** program in **UniverseMachine** to walk through all the Bolshoi-Planck **hlist** files, yielding the main progenitor information of every subhalo that was ever identified by **Consistent Trees**.

Since it is likely that some portion of these disrupted subhalos should be populated with model galaxies (Guo & White 2014; Campbell et al. 2017), in our initial application of deconvolution abundance matching we derive the  $M_{\star} - M_{\text{peak}}$  relation using *all* subhalos, including those that may be disrupted. We then apply a selection function to the disrupted subhalos, so that a fraction of these objects will host galaxies in our mock universe. We refer to this as the *orphan selection function*,  $\mathcal{F}_{\text{orphan}}$ , which we consider to be an integral component of our application of abundance matching.

Since a rigorous calibration of  $\mathcal{F}_{\text{orphan}}$  is beyond the scope of the present work, we instead opt for a simple parameterization that yields reasonably accurate recovery of the galaxy clustering signal observed in SDSS. We model  $\mathcal{F}_{\text{orphan}} = \mathcal{F}_{\text{orphan}}(M_{\text{peak}}, M_{\text{host}})$ , where  $M_{\text{peak}}$  is the peak mass of the disrupted subhalo, and  $M_{\text{host}}$  is the present-day virial mass of its  $z = 0$  host halo. For the  $M_{\text{peak}}$ -dependence, we select 50% of disrupted subhalos with  $M_{\text{peak}} = 10^{11} M_{\odot}$ , 0% of subhalos with  $M_{\text{peak}} = 10^{13} M_{\odot}$ , linearly interpolating in  $\log M_{\text{peak}}$  for intermediate values of  $M_{\text{peak}}$ . At each  $M_{\text{peak}}$ , the selec-

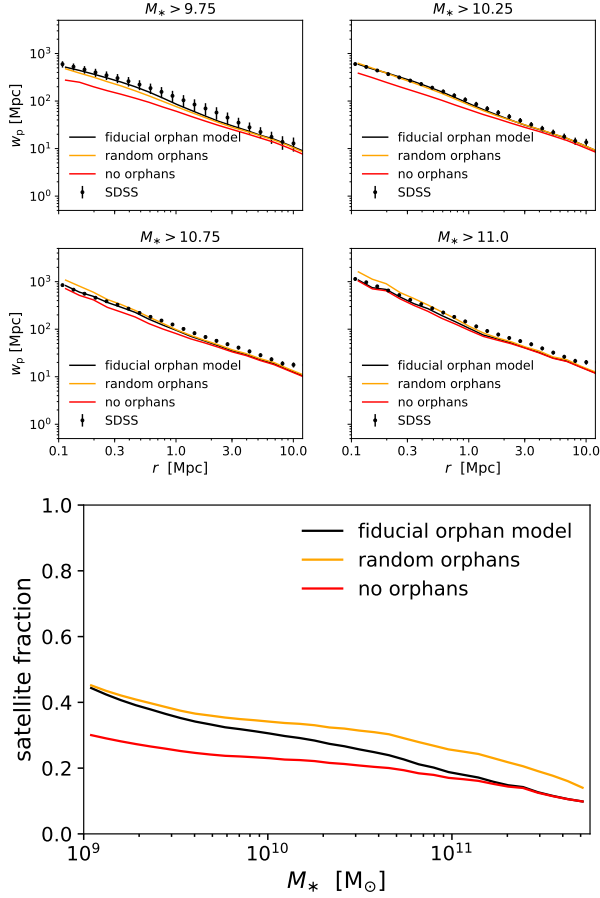


**Figure 11. Impact of the orphan selection function.** The *top panel* is identical to Figure 2, but includes additional curves for the case of randomly selected orphan halos (orange curves), and no orphans at all (red curves). As a function of stellar mass, the *bottom panel* shows the satellite fraction, i.e., the fraction of objects that are not central galaxies.

tion of disrupted halos is not random; instead, we preferentially select the subhalos with larger  $M_{\text{host}}$ , which we intend to offset the increased difficulty of subhalo-finding algorithms to identify subhalos with especially small values of  $\mu \equiv M_{\text{peak}}/M_{\text{host}}$ . We refer to this model as our “fiducial orphan model”. We assess the role of the non-trivial features in  $\mathcal{F}_{\text{orphan}}$  by randomly selecting the same number of orphan subhalos, referring to this alternate model as the “random orphan model”.

Figure 11 illustrates the impact of the orphan selection function on  $M_*$ -threshold clustering (top panel) and the satellite fraction (bottom panel). Comparing the black to the red curves shows that including orphans substantially boosts small-scale clustering due to the increased satellite fraction. Comparing the orange to the black curves, we see that randomly selecting orphans results in excessive small-scale clustering for the higher-mass threshold samples due to the inclusion of too many disrupted subhalos with large values of  $M_{\text{peak}}$ .